Wave propagation in anisotropic, saturated porous media: Plane-wave theory and numerical simulation

José M. Carcione[a)]

Osservatorio Geofisico Sperimentale, P.O. Box 2011 Opicina, 34016 Trieste, Italy

Porous media are anisotropic due to bedding, compaction, and the presence of aligned microcracks and fractures. Here, it is assumed that the skeleton (and not the solid itself) is anisotropic. The rheological model also includes anisotropic tortuosity and permeability. The poroelastic equations are based on a transversely isotropic extension of Biot's theory, and the problem is of plane strain type, i.e., two dimensional, describing $qP-qS$ propagation. In the high-frequency case, the (two) viscodynamic operators are approximated by Zener relaxation functions that allow a closed differential formulation of Biot's equation of motion. A plane-wave analysis derives expressions for the slowness, attenuation, and energy velocity vectors, and quality factor for homogeneous viscoelastic waves. The slow wave shows an anomalous polarization behavior. In particular, when the medium is strongly anisotropic the polarization is quasishear and the wave presents cuspidal triangles. Anisotropic tortuosity affects mainly the slow wavefront, and anisotropic permeability produces strong anisotropic attenuation of the three modes. The diffusive characteristics of the slow mode are predicted by the plane-wave analysis. As in the single-phase case, it is confirmed that the phase velocity is the projection of the energy velocity vector onto the propagation direction. Moreover, some fundamental energy relations, valid for a single-phase medium, are generalized to two-phase media. Transient propagation is solved with a direct grid method and a time-splitting integration algorithm, allowing the solution of the stiff part of the differential equations in closed analytical form. The snapshots show that the three waves are propagative when the fluid is ideal (zero viscosity). It is confirmed that, when the fluid is viscous, the slow wave becomes diffusive and appears as a static mode at the source location. The modeling confirms the triplication (cusps) of the slow wave and the polarization behavior predicted by the plane analysis. © *1996 Acoustical Society of America.*

PACS numbers: 43.20.Bi, 43.20.Jr, 43.30.Ma, 43.40.Ph

INTRODUCTION

The concepts of porous and fractured media have gained much attention in recent years. The applications cover a variety of fields, from physics to geophysics, engineering and soil mechanics, underwater acoustics, etc.[1–3] In particular, in the exploration of oil and gas reservoirs, it is important to predict the preferential directions of fluid flow. These are closely related to the permeability of the medium, and consequently to the geometric characteristics of the skeleton. That is to say, an anisotropic skeleton implies that permeability is anisotropic and vice versa. For instance, shales are naturally bedded and possess intrinsic anisotropy at the microscopic level. Similarly, compaction and the presence of microcracks and fractures make the skeleton anisotropic.

The constitutive equations for anisotropic porous media were first given by Biot[4,5] and Biot and Willis.[6] More recently, Thompson and Willis[7] reformulated the stress-strain equations in terms of measurable quantities, and Badiey *et al.*[8] applied these concepts to wave propagation in a transversely isotropic seafloor (see also Coussy[3]). This theory, used here to describe the medium, assumes that the solid constituent is isotropic and that the anisotropy is solely due to the arrangement of the grains (i.e., the skeleton is anisotropic). An alternative approach to obtain an anisotropic poroelastic medium was presented by Norris,[9] who applied Backus theory to a periodically layered system composed of isotropic Biot constituents. The effects of anisotropic permeability on the kinematics of wave propagation were investigated in Ben-Menahem and Gibson,[10] and Gelinsky and Shapiro.[11,12] They found that the degree of attenuation and velocity anisotropy is strongly dependent on the frequency range.

The poroelastic equations of motion combine the constitutive relations with the equations of momentum conservation and the dynamic Darcy's law in the framework of Biot's theory. The theory assumes that the medium is isotropic in the bedding plane (say, the x-y plane), and anisotropic in the x-z plane. Then, the stress-strain relations are transversely isotropic, and Darcy's law is described by two permeability constants.[13] In order to simulate wave propagation in the low- and high-frequency ranges, a time domain formulation of the viscodynamic operator is introduced. A different relaxation function is assigned to each principal permeability. For high frequencies, the formulation requires the introduction of hidden variables that circumvent the convolutional relations imposed by the time domain approach. The numerical solution is computed with a direct grid method based on the Fourier pseudospectral operator. Since the presence of

[a)]Tel: 0039-40-2140345, Fax: +39 40 327307, E-mail: carcione@gems755.ogs.trieste.it

the slow compressional wave makes Biot's differential equations stiff,[14] a time splitting time integration algorithm is used. The stiff part is solved analytically, and the nonstiff part by using a high-order explicit scheme. The resulting algorithm posseses 4th-order accuracy in time, and ''infinite'' (spectral) accuracy in space.

The paper is organized as follows. Section I presents the stress-strain relations. Then, Sec. II gives the dynamical equations and Darcy's law generalized to the anisotropic case and including the viscodynamic operator in the time domain. The low- and high-frequency range time domain equations are explicitly given in Sec. III as first-order differential equations in time. In order to obtain a physical insight of the wave processes prior to the numerical solution of the wave equation, a plane-wave analysis is presented in Sec. IV, where slowness, attenuation, and energy velocity curves are calculated. The numerical solution algorithm is developed in Sec. V and, finally, Sec. VI presents the theoretical results and simulations.

Summarizing, the contributions of the present paper are the following: (i) recasting Biot differential equations in the time-domain including low- and high-frequency phenomena, (ii) a plane-wave analysis for poroelastic anisotropic media based on energy considerations, (iv) the use of a splitting time-integration technique to overcome the stiffness of Biot equations, and (v) the numerical solution of Biot anisotropic equations by a direct grid method based on a pseudospectral differential operator.

I. STRESS-STRAIN RELATIONS

The constitutive equations for an inhomogeneous, transversely isotropic poroelastic medium under plane strain conditions are given by[8]

$$\partial_t \tau_{xx} = c_{11}^u \ \partial_x v_x + c_{13}^u \ \partial_z v_z + \alpha_1 M(\partial_x q_x + \partial_z q_z) + \partial_t s_{11},$$
(1)

$$\partial_t \tau_{zz} = c_{13}^u \ \partial_x v_x + c_{33}^u \ \partial_z v_z + \alpha_3 M(\partial_x q_x + \partial_z q_z) + \partial_t s_{33},$$
(2)

$$\partial_t \tau_{xz} = c_{55}^u (\partial_z v_x + \partial_x v_z) + \partial_t s_{55},$$
(3)

$$\partial_t p = -\alpha_1 M \ \partial_x v_x - \alpha_3 M \ \partial_z v_z - M(\partial_x q_x + \partial_z q_z) + \partial_t s_f,$$
(4)

where τ_{xx}, τ_{zz}, and τ_{xz} are the total stresses, p is the fluid pressure, the v's and the q's are the solid and fluid (relative to the solid) particle velocities, respectively, c_{IJ}^u, $I,J=1,...,6$ are the undrained elastic components, M is an elastic modulus, and α_i, $i=1,3$ are Biot's effective coefficients. Moreover, s_{IJ} and s_f are the solid and fluid external sources, respectively. The conventions are that ∂_t denotes time differentiation, and that ∂_x and ∂_z are the spatial derivative operators.

The drained elastic components c_{IJ} are obtained for $p=0$ (jacketed test on a dry sample). The relations with the undrained components are

$$c_{11}^u = c_{11} + \alpha_1^2 M,$$
(5)

$$c_{33}^u = c_{33} + \alpha_3^2 M,$$
(6)

$$c_{13}^u = c_{13} + \alpha_1 \alpha_3 M,$$
(7)

$$c_{55}^u = c_{55}.$$
(8)

The theory assumes that the anisotropy of the porous frame is mainly caused by the directional arrangement of the grains, and not by the anisotropy of the individual grains. In this case, the effective coefficients are given by[8]

$$\alpha_1 = 1 - \frac{c_{11} + c_{12} + c_{13}}{3K_s},$$
(9)

$$\alpha_3 = 1 - \frac{2c_{13} + c_{33}}{3K_s},$$
(10)

where K_s is the bulk modulus of the grains.

An undrained test[8] gives the modulus M:

$$M = \frac{K_s^2}{D - (2c_{11} + c_{33} + 2c_{12} + 4c_{13})/9},$$
(11)

where

$$D = K_s[1 + \phi(K_s K_f^{-1} - 1)],$$
(12)

with K_f the fluid bulk modulus and ϕ the porosity.

Then, the stress-strain relation are completely determined from the following material properties obtained from experiments: the drained elastic moduli c_{IJ}, the solid and fluid moduli K_s and K_f, and the porosity ϕ.

To illustrate the role of the various anisotropic coefficients, consider the isotropic case.[15] Isotropy implies that

$$c_{11}^u = c_{33}^u = H = K_m + \frac{4}{3}\mu + \frac{(K_s - K_m)^2}{D - K_m},$$

$$c_{12}^u = c_{13}^u = H - 2\mu,$$
(13)

$$c_{11} = c_{33} = K_m + \tfrac{4}{3}\mu, \quad c_{12} = c_{13} = K_m - \tfrac{2}{3}\mu,$$
(14)

$$c_{55}^u = c_{55} = \mu,$$
(15)

$$\alpha_1 = \alpha_3 = \alpha = 1 - K_m/K_s,$$
(16)

where K_m and μ are the bulk and shear moduli of the (drained) matrix, respectively, and

$$M = \frac{K_s^2}{D - K_m}.$$
(17)

In Biot,[15] the quantity αM is denoted by C, and the undrained bulk modulus is $H - 4\mu/3$. Note that the properties of the fluid enter through the parameter D.

II. DYNAMICAL EQUATIONS AND DARCY'S LAW

The dynamical equations describing wave propagation in heterogeneous porous media were obtained by Biot.[15] For plane strain conditions they are

$$\partial_x \tau_{xx} + \partial_z \tau_{xz} = \rho \ \partial_t v_x + \rho_f \ \partial_t q_x,$$
(18)

$$\partial_x \tau_{xz} + \partial_z \tau_{zz} = \rho \ \partial_t v_z + \rho_f \ \partial_t q_z,$$
(19)

where $\rho = (1-\phi)\rho_s + \phi\rho_f$ is the composity density, with ρ_s and ρ_f the solid and fluid densities.

On the other hand, it is assumed that the dynamic Darcy's law, generalized to the anisotropic case, can be expressed as

$$-\partial_x p = \rho_f \, \partial_t v_x + \psi_1 * \partial_t q_x, \tag{20}$$

$$-\partial_z p = \rho_f \, \partial_t v_z + \psi_3 * \partial_t q_z, \tag{21}$$

where the asterisk denotes time convolution, and ψ_i, $i=1,3$ are time-dependent functions such that Biot's viscodynamic operators for the x and z directions are given by

$$Y_i(\omega) = \mathcal{F}[\partial_t \psi_i], \tag{22}$$

with the operator $\mathcal{F}$ denoting the time Fourier transform. In the low-frequency range,[16] i.e., for frequencies lower than $\omega_c = \min(\omega_i)$, where $\omega_i = \eta/(m_i \kappa_i)$,

$$\psi_i(t) = m_i \delta(t) + (\eta/\kappa_i)H(t), \tag{23}$$

where $m_i = T_i \rho_f / \phi$, with T_i the tortuosity, η is the fluid viscosity, κ_i, $i=1,3$ are the principal components of the global permeability tensor, $\delta(t)$ is Dirac's function, and $H(t)$ is the Heaviside function. From Eq. (22),

$$Y_i(\omega) = \iota \omega m_i + \eta/\kappa_i, \tag{24}$$

where $\iota = \sqrt{-1}$. In terms of mechanical models, Eq. (23) represents a Kelvin–Voigt element.[17] Substitution of Eq. (23) into Eqs. (20) and (21) gives Biot's dynamic Darcy's law in the low-frequency range:[16]

$$-\partial_x p = \rho_f \, \partial_t v_x + m_1 \, \partial_t q_x + (\eta/\kappa_1)q_x, \tag{25}$$

$$-\partial_z p = \rho_f \, \partial_t v_z + m_3 \, \partial_t q_z + (\eta/\kappa_3)q_z. \tag{26}$$

In the high-frequency range ($\omega \geq \omega_c$), the viscodynamic operator is strongly influenced by the pore geometry, and a precise evaluation of its frequency dependence requires an experimental determination.[18] For high frequencies, the time-domain viscodynamic operator is approximated by the following generalized Zener kernel:[19]

$$\psi_i(t) = \psi_i^0 \left[1 - \frac{1}{L_i} \sum_{l=1}^{L_i} \left(1 - \frac{\lambda_{il}}{\tau_{il}} \right) \exp(-t/\tau_{il}) \right] H(t),$$

$$i = 1 \text{ or } 3, \tag{27}$$

where ψ_i^0 is the relaxed value ($t \to \infty$), λ_{il} and τ_{il} are relaxation times ($\lambda_{il} \geq \tau_{il}$), and L_i is the number of Zener elements. In general, for a smooth time dependence, two or three elements suffice to get a fairly good approximation, as in the case of viscoelastic modeling with a nearly constant quality factor.[21] Since, as it is shown below, each element adds a new first-order differential equation, this implies more computer storage and time.

The high-frequency limit is obtained for $t \to 0$. It gives

$$\psi_i^\infty = \frac{\psi_i^0}{L_i} \sum_{l=1}^{L_i} \frac{\lambda_{il}}{\tau_{il}}. \tag{28}$$

Equation (22) applied to (27) gives the expression of the high-frequency viscodynamic operator:

$$Y_i(\omega) = \frac{\psi_i^0}{L_i} \sum_{l=1}^{L_i} \frac{1 + \iota \omega \lambda_{il}}{1 + \iota \omega \tau_{il}}. \tag{29}$$

The range of validity of $Y_i(\omega)$ is defined by the lower limit ω_c and, for this frequency, the following constraints can be imposed:

$$\mathrm{Re}[Y_i(\omega_c)] = \eta/\kappa_i, \tag{30}$$

and

$$\mathrm{Im}[Y_i(\omega_c)] = \omega_c m_i, \tag{31}$$

that satisfy the continuity between the low- and high-frequency ranges. The operators $\mathrm{Re}(\cdot)$ and $\mathrm{Im}(\cdot)$ take real and imaginary parts, respectively. On the other hand, when $\omega \to \infty$, the operator Y_i and Biot's theory loose their physical meanings, since scattering takes place (the theory is valid when the wavelength is large compared to the dimensions of the pores).

Equations (1)–(4), (18), (19), (20), and (21) could be the basis for a numerical solution algorithm. However, numerical evaluation of the convolution integrals is prohibitive when solving the differential equations with grid methods and explicit time evolution techniques (the low-frequency case poses no problem, since substitution of Eq. (23) into Eqs. (20) and (21) does not involve time convolutions). In order to circumvent the convolutions due to the high-frequency kernels, a new set of field variables is introduced. Consider the terms $\psi_i * \partial_t q_m$ in Eqs. (20) and (21), where $m=1$ and $m=3$ denote the x and z coordinates. With the use of convolution properties, this term can be written as

$$\psi_i * \partial_t q_m = \psi_i^\infty q_m + \psi_i^0 \sum_{l=1}^{L_i} e_{il}, \tag{32}$$

where

$$e_{il} = \xi_{il} * q_m \tag{33}$$

are hidden variables, with

$$\xi_{il}(t) = \frac{H(t)}{L_i \tau_{il}} \left(1 - \frac{\lambda_{il}}{\tau_{il}} \right) \exp\left(\frac{-t}{\tau_{il}} \right). \tag{34}$$

Substituting Eq. (32) into Eqs. (20) and (21) gives

$$-\partial_x p = \rho_f \, \partial_t v_x + \psi_1^\infty q_x + \psi_1^0 \sum_{l=1}^{L_1} e_{1l}, \tag{35}$$

and

$$-\partial_z p = \rho_f \, \partial_t v_z + \psi_3^\infty q_z + \psi_3^0 \sum_{l=1}^{L_3} e_{3l}. \tag{36}$$

The formulation is completed with the differential equations corresponding to the hidden variables. Time differentiation of Eq. (33) and use of convolution properties yields

$$\frac{\partial e_{il}}{\partial t} = -\frac{1}{\tau_{il}} e_{il} + \xi_{il}(0)q_m, \tag{37}$$

where the pair (i,m) corresponds to $(1,x)$ or $(3,z)$. The dynamical equations are completely defined in terms of the following parameters: the densities ρ_s and ρ_f, the porosity ϕ, the viscosity η, the tortuosities T_i, the permeabilities κ_i, the constants ψ_i^0, and the set of relaxation times $(\lambda_{il}, \tau_{il})$, $l=1,\ldots,L_i$.

TABLE I. Material properties.

Material	Property	Sandstone	Epoxy–glass	Unit
Solid	bulk modulus, K_s	80.	40.	GPa
	density, ρ_s	2500.	1815.	kg/m^3
Matrix	elasticity, c_{11}	71.8	39.4	GPa
	elasticity, c_{12}	3.2	1.	⋯
	elasticity, c_{13}	1.2	5.8	⋯
	elasticity, c_{33}	53.4	13.1	⋯
	elasticity, c_{55}	26.1	3.	⋯
	porosity, ϕ	0.2	0.2	
	permeability, κ_1	600.	600.	mD
	permeability, κ_3	100.	100.	⋯
	tortuosity, T_1	2.	2.	
	tortuosity, T_3	3.6	3.6	
Fluid	bulk modulus, K_f	2.5	2.5	GPa
	density, ρ_f	1040.	1040.	kg/m^3
	viscosity, η	1.	1.	cP

III. THE WAVE EQUATIONS

The following is the velocity-stress formulation of the low- and high-frequency range poroelastic equations.

A. Low-frequency range

Equations (18), (19), (25), and (26) yield

$$\partial_t v_x = \beta_{11}^{(1)}(\partial_x \tau_{xx} + \partial_z \tau_{xz}) - \beta_{12}^{(1)}\left(\partial_x p + \frac{\eta}{\kappa_1} q_x\right), \quad (38)$$

$$\partial_t v_z = \beta_{11}^{(3)}(\partial_x \tau_{xz} + \partial_z \tau_{zz}) - \beta_{12}^{(3)}\left(\partial_z p + \frac{\eta}{\kappa_3} q_z\right), \quad (39)$$

$$\partial_t q_x = \beta_{21}^{(1)}(\partial_x \tau_{xx} + \partial_z \tau_{xz}) - \beta_{22}^{(1)}\left(\partial_x p + \frac{\eta}{\kappa_1} q_x\right), \quad (40)$$

$$\partial_t q_z = \beta_{21}^{(3)}(\partial_x \tau_{xz} + \partial_z \tau_{zz}) - \beta_{22}^{(3)}\left(\partial_z p + \frac{\eta}{\kappa_3} q_z\right), \quad (41)$$

where

$$\begin{bmatrix} \beta_{11}^{(i)} & \beta_{12}^{(i)} \\ \beta_{21}^{(i)} & \beta_{22}^{(i)} \end{bmatrix} = (\rho_f^2 - \rho m_i)^{-1} \begin{bmatrix} -m_i & \rho_f \\ \rho_f & -\rho \end{bmatrix}. \quad (42)$$

The wave equation is completed with Eqs. (1)–(4).

B. High-frequency range

Equations (18), (19), (35), and (36) yield

$$\partial_t v_x = -\frac{1}{\rho_f}\left(\partial_x p + \psi_1^\infty q_x + \psi_1^0 \sum_{l=1}^{L_1} e_{1l}\right), \quad (43)$$

$$\partial_t v_z = -\frac{1}{\rho_f}\left(\partial_z p + \psi_3^\infty q_z + \psi_3^0 \sum_{l=1}^{L_3} e_{3l}\right), \quad (44)$$

$$\partial_t q_x = \frac{1}{\rho_f}\left[(\partial_x \tau_{xx} + \partial_z \tau_{xz}) + \frac{\rho}{\rho_f}\left(\psi_1^\infty q_x + \psi_1^0 \sum_{l=1}^{L_1} e_{1l}\right)\right], \quad (45)$$

$$\partial_t q_z = \frac{1}{\rho_f}\left[(\partial_x \tau_{xz} + \partial_z \tau_{zz}) + \frac{\rho}{\rho_f}\left(\psi_3^\infty q_z + \psi_3^0 \sum_{l=1}^{L_3} e_{3l}\right)\right]. \quad (46)$$
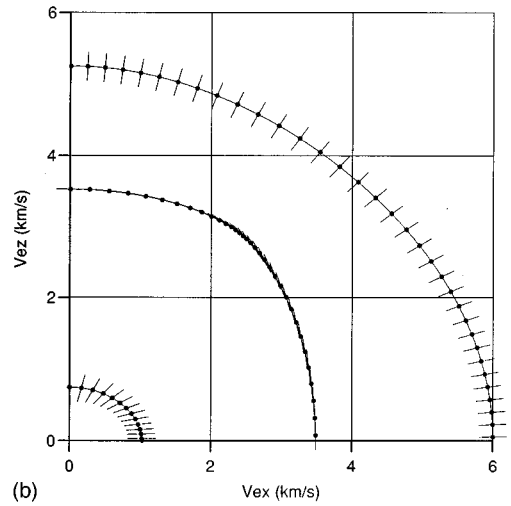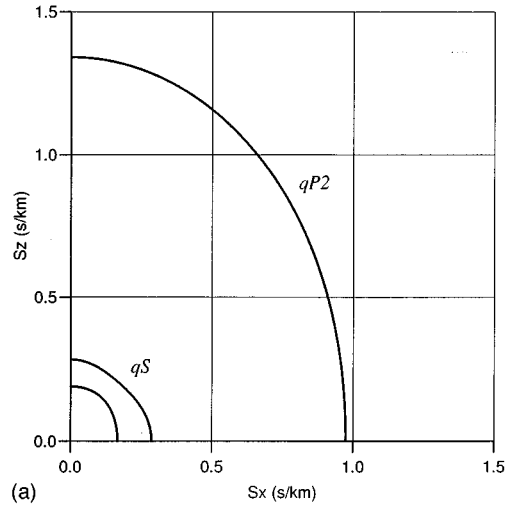

FIG. 1. Polar representations of (a) the slowness curves and (b) the energy velocity curves for $\eta=0$, corresponding to the sandstone. Only one quarter of the curves are displayed because of symmetry considerations. The tick-marks indicate the polarization directions, with the points uniformly sampled as a function of phase angle. Referring to (b), the outer curve corresponds to the fast quasicompressional wave qP_1; then follows the quasishear wave qS and the slow quasicompressional wave qP_2 (inner curve). The opposite order applies to the slowness curves.

The wave equation is completed with Eqs. (1)–(4) and (37).

IV. PLANE-WAVE THEORY

A general plane-wave solution for the particle velocity vector

$$\mathbf{V} \equiv [v_x, v_z, q_x, q_z]^{\mathsf{T}} \quad (47)$$

is

$$\mathbf{V} = \mathbf{V}_0 \exp[\iota(\mathbf{k}\cdot\mathbf{x} - \omega t)], \quad (48)$$

where $\mathbf{V}_0$ represents a constant complex vector and $\mathbf{k}$ is the wave vector. For homogeneous waves, the wave vector can be written as

$$\mathbf{k} \equiv \boldsymbol{\kappa} - \iota\boldsymbol{\alpha} = (\kappa - \iota\alpha)\hat{\boldsymbol{\kappa}} \equiv k\hat{\boldsymbol{\kappa}}, \quad (49)$$
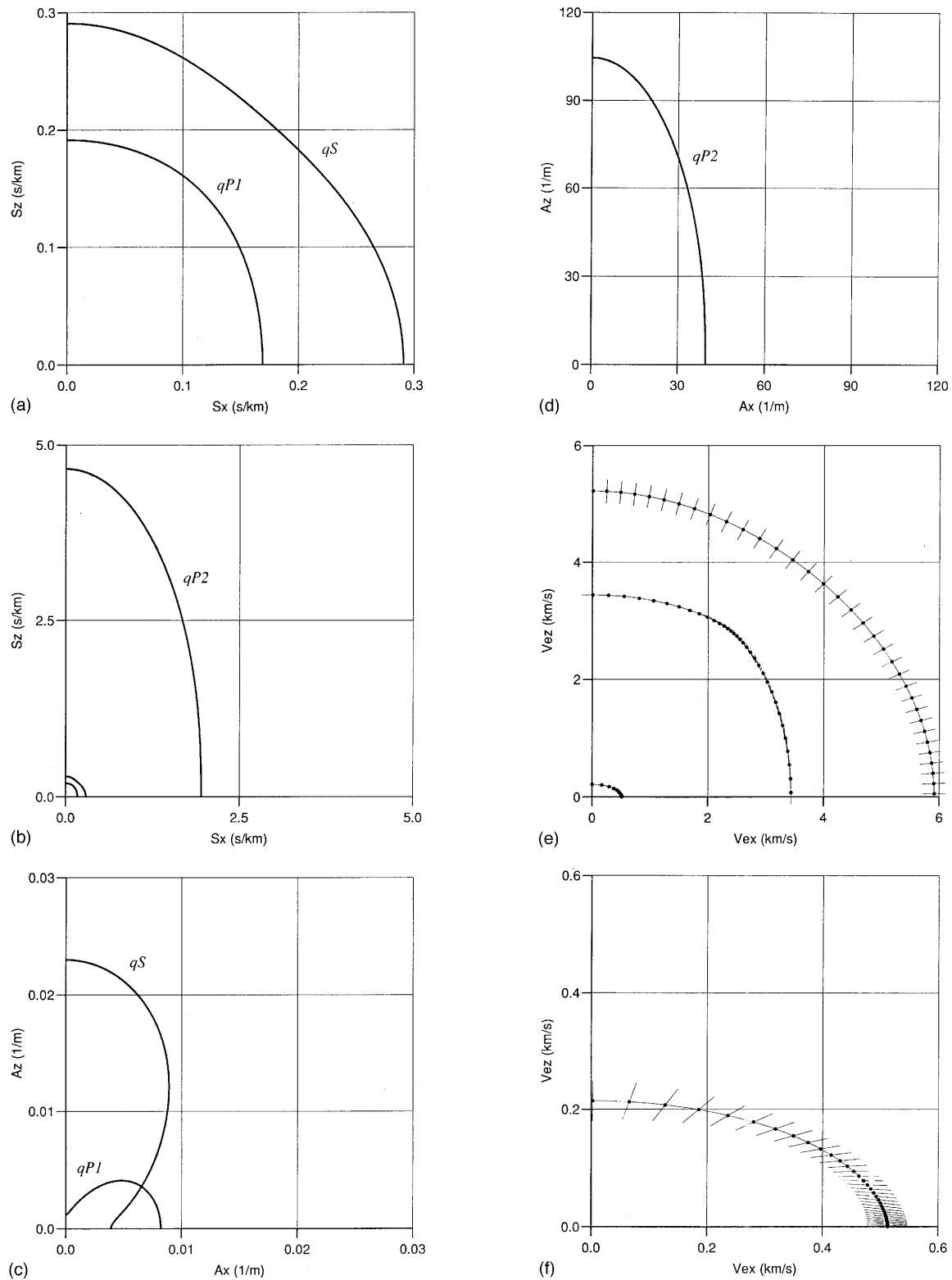
where

FIG. 2. Slowness, attenuation and energy velocity curves for sandstone and $\eta \neq 0$, where (a) and (b) show the slownesses, (c) and (d) the attenuations, and (e) and (f) the energy velocities. The curves correspond to a frequency of 3730 Hz, which is the central frequency of the source used for the numerical simulation.

$$\hat{\boldsymbol{\kappa}} = l_x \hat{\mathbf{e}}_x + l_z \hat{\mathbf{e}}_z \tag{50}$$

defines the propagation direction through the directions cosines l_x and l_z.

Defining the stress vector as

$$\mathbf{T} \equiv [\tau_{xx}, \tau_{zz}, \tau_{xz}, -p]^\mathsf{T} \tag{51}$$

and substituting the plane wave (48) into the stress-strain relations (1)–(5) yields

$$-\omega \mathbf{T} = k \mathbf{C} \cdot \mathbf{V}, \tag{52}$$
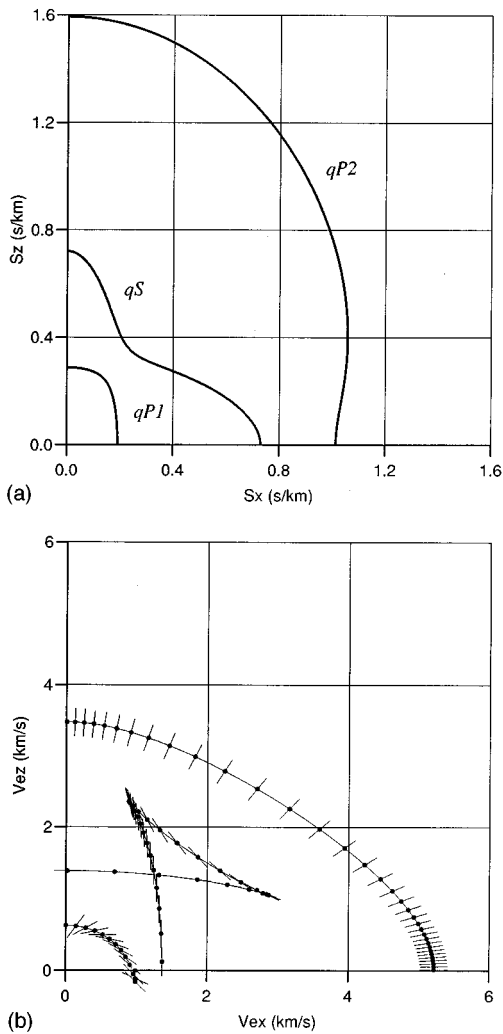
where

FIG. 3. Polar representations of (a) the slowness curves and (b) the energy velocity curves for $\eta=0$, corresponding to the epoxy–glass porous medium. Only one quarter of the curves are displayed because of symmetry considerations. The tickmarks indicate the polarization directions, with the points uniformly sampled as a function of phase angle.

$$\mathbf{C}=\begin{bmatrix} l_x c^u_{11} & l_z c^u_{13} & \alpha_1 M l_x & \alpha_1 M l_z \\ l_x c^u_{13} & l_z c^u_{33} & \alpha_3 M l_x & \alpha_3 M l_z \\ l_z c^u_{55} & l_x c^u_{55} & 0 & 0 \\ \alpha_1 M l_x & \alpha_3 M l_z & M l_x & M l_z \end{bmatrix} \tag{53}$$

and zero external forces have been assumed.

On the other hand, for the plane wave (48) the dynamical equations (18) and (19) and Darcy's law (20) and (21) can be expressed in matrix form as

$$k\mathbf{L}\cdot\mathbf{T}=-\omega\mathbf{\Gamma}\cdot\mathbf{V}, \tag{54}$$

where

$$\mathbf{L}=\begin{bmatrix} l_x & 0 & l_z & 0 \\ 0 & l_z & l_x & 0 \\ 0 & 0 & 0 & l_x \\ 0 & 0 & 0 & l_z \end{bmatrix} \tag{55}$$

and

$$\mathbf{\Gamma}=\begin{bmatrix} \rho & 0 & \rho_f & 0 \\ 0 & \rho & 0 & \rho_f \\ \rho_f & 0 & \iota Y_1(-\omega)/\omega & 0 \\ 0 & \rho_f & 0 & \iota Y_3(-\omega)/\omega \end{bmatrix}. \tag{56}$$

Equations (52) and (54) give

$$\left(\mathbf{\Gamma}^{-1}\cdot\mathbf{L}\cdot\mathbf{C}-\frac{\omega^2}{k^2}\,\mathbf{I}_4\right)\cdot\mathbf{V}=0, \tag{57}$$

where $\mathbf{I}_4$ denotes the four-dimensional unit matrix. By making zero the determinant, Eq. (57) gives the following dispersion relation:

$$\det(\mathbf{\Gamma}^{-1}\cdot\mathbf{L}\cdot\mathbf{C}-V^2\mathbf{I}_4)=0, \tag{58}$$

where

$$V=\omega/k \tag{59}$$

is the complex velocity. The eigensystem formed by Eqs. (57) and (58) gives four eigenvalues and the corresponding eigenvectors. Three of them correspond to the wave modes, and the fourth equals zero since it can be shown that two rows of the system matrix are linearly dependent.

The slowness and attenuation vectors can be expressed in terms of the complex velocity as

$$\mathbf{s}=\mathrm{Re}(1/V)\hat{\boldsymbol{\kappa}} \tag{60}$$

and

$$\boldsymbol{\alpha}=\omega\,\mathrm{Im}(1/V)\hat{\boldsymbol{\kappa}}, \tag{61}$$

respectively.

The wavefront is the locus of the end of the energy velocity vector multiplied by one unit of propagation time, with the energy velocity defined as the ratio of the average power flow density $\langle\mathbf{P}\rangle$ to the mean energy density $\langle E\rangle$. Since this is equal to the sum of the average kinetic and strain energy densities $\langle T\rangle$ and $\langle W\rangle$, the energy velocity is

$$\mathbf{V}_e=\frac{\langle\mathbf{P}\rangle}{\langle T+W\rangle}, \tag{62}$$

where $\mathbf{P}$ is the Umov–Poynting vector and the operation $\langle\cdot\rangle$ is the averaged value over one cycle of harmonic oscillations.

Dissipation can also be quantified by the quality factor, which is defined as

$$Q=2\langle W\rangle/\langle D\rangle, \tag{63}$$

where $\langle D\rangle$ is the dissipated energy density.

The calculation of the energy balance equation, Umov–Poynting vector, and energy densities, in terms of the eigensystem obtained from Eq. (57), is given in the Appendix. The energy balance equation, also called the Umov–Poynting theorem, is

$$-\boldsymbol{\alpha}^\mathsf{T}\cdot\mathbf{P}=\iota\omega[\langle W\rangle-\langle T\rangle]-\omega\langle D\rangle. \tag{64}$$

Moreover, the two fundamental relations

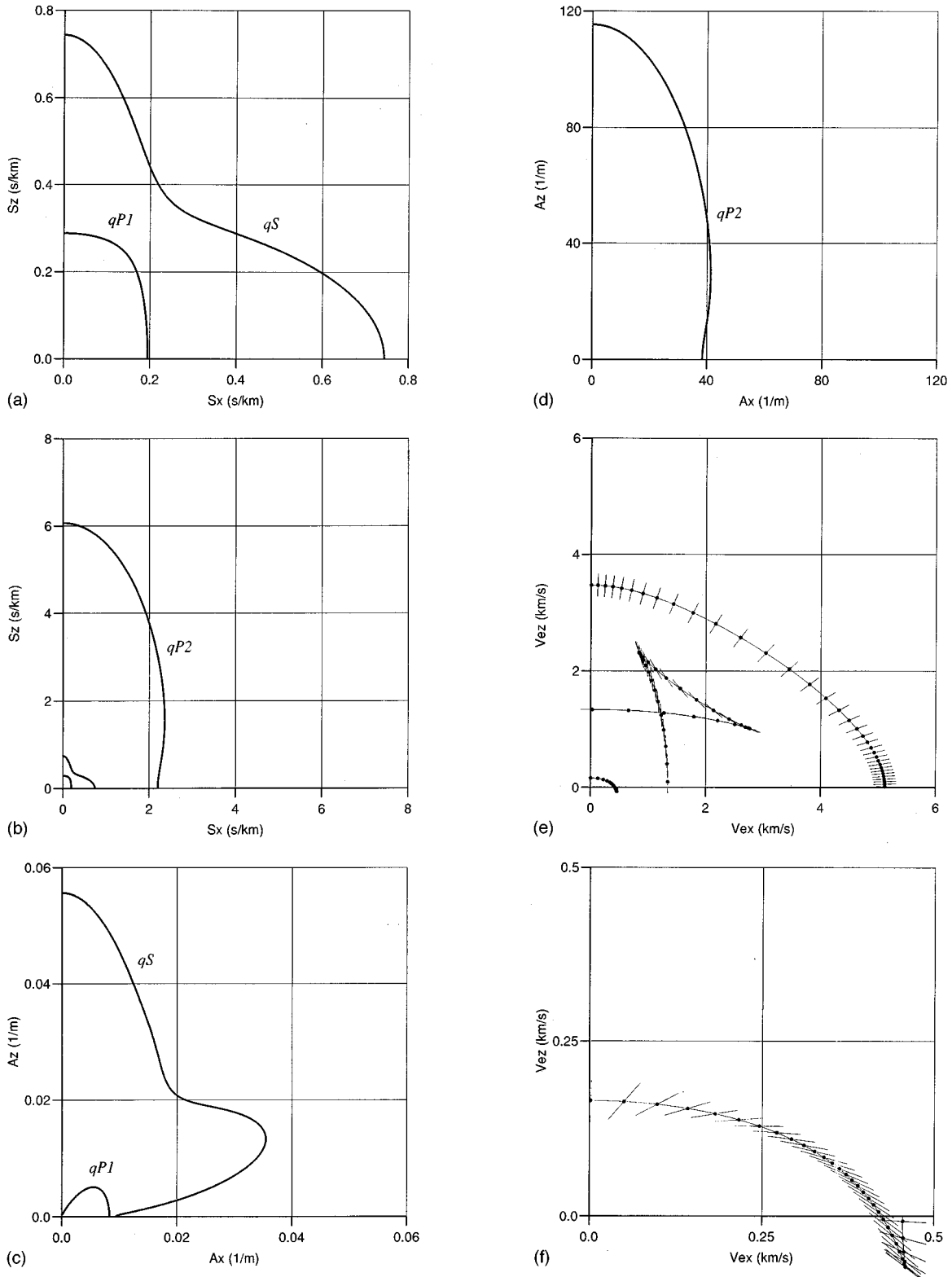$$\hat{\boldsymbol{\kappa}}^\mathsf{T}\cdot\mathbf{V}_e=V_p \tag{65}$$

and

FIG. 4. Slowness, attenuation and energy velocity curves for the epoxy–glass system and $\eta \neq 0$, where (a) and (b) show the slownesses, (c) and (d) the attenuations, and (e) and (f) the energy velocities. The curves correspond to a frequency of 3135 Hz, which is the central frequency of the source used for the numerical simulation.

$$\boldsymbol{\alpha}^{\mathrm{T}} \cdot \langle \mathbf{P} \rangle = \omega \langle D \rangle, \tag{66}$$

where $V_p = \omega/\kappa$ is the phase velocity, are obtained in the Appendix. These are generalizations, to two-phase media, of similar equations for single-phase anisotropic-viscoelastic media.[20] In particular, Eq. (65) means that the phase velocity is the projection of the energy velocity onto the propagation direction.
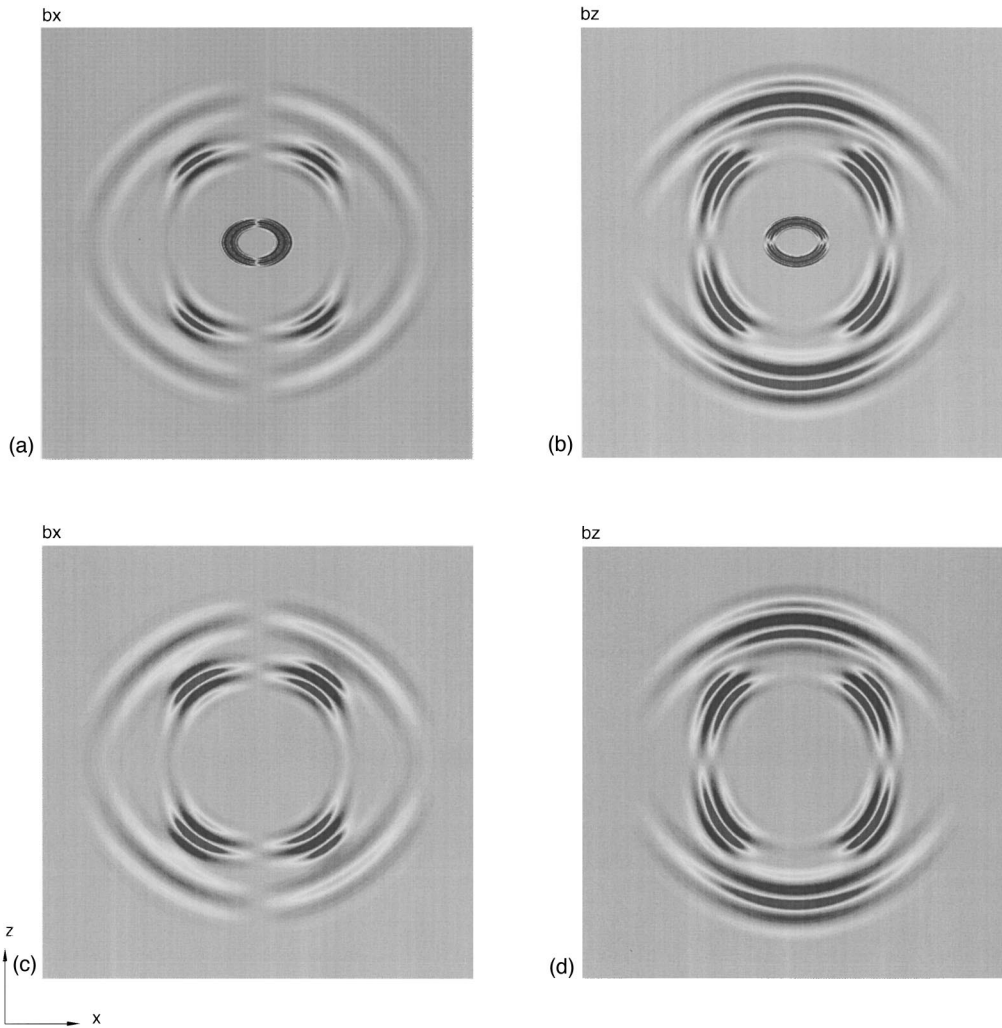
FIG. 5. Snapshots (not scaled) of the center of mass particle velocity components at 1.56-ms propagation time, where (a) and (b) correspond to $\eta=0$, and (c) and (d) to $\eta\neq0$. The medium is sandstone. Three events can be observed, the fast qP_1 wave (outer wavefront), the qS wave and the slow qP_2 wave (inner wavefront).

V. NUMERICAL SOLUTION ALGORITHM

The system of equations describing wave motion can be written in matrix form as

$$\partial_t \mathbf{W} = \mathbf{M}\mathbf{W} + \mathbf{S}, \tag{67}$$

where

$$\mathbf{W} = [v_x, v_z, q_x, q_z, \tau_{xx}, \tau_{zz}, \tau_{xz}, p, e_{1l}, e_{3l}]^{\mathsf{T}} \tag{68}$$

is the unknown field vector (the hidden variables only appear in the high-frequency case), $\mathbf{M}$ is the propagation matrix, which contains the spatial derivatives and material properties, and

$$\mathbf{S} = \partial_t[0,0,0,0,s_{11},s_{33},s_{55},s_f,0,0]^{\mathsf{T}} \tag{69}$$

is the source vector.

Consider the 1-D version of Eq. (67) with $\mathbf{S}=0$. The plane wave

$$\mathbf{W} = \mathbf{W}_0 \, \exp[\iota(\omega_C t - kx)], \tag{70}$$

where ω_C is the complex frequency and k is the wave number, is a solution and gives an eigenvalue equation for the

eigenvalues $\lambda = \iota\omega_C$ (see Carcione[21]). When using the Fourier pseudospectral method for computing the spatial derivatives, the wave numbers supported by the numerical mesh span from $k=0$ to the Nyquist wave number $k=\pi/D_X$, where D_X is the grid spacing. It can be shown that the eigenvalues come in complex conjugate pairs.[22] When the fluid viscosity is zero, they lie on the imaginary axis, and describe propagating modes without dissipation. For a viscous fluid, the eigenvalues have a negative real part meaning that the waves are attenuated, in particular the slow wave. More precisely, the largest negative eigenvalue corresponds to the slow wave for $k=0$:

$$\lambda_s^{(1)} = -(\eta/\kappa_1)\beta_{22}^{(1)}. \tag{71}$$

In order to have numerical stability, the domain of convergence of the time integration scheme should include this eigenvalue. For instance, an explicit 4th-order Runge–Kutta method[14] requires $dt\lambda_s^{(1)} > -2.78$, implying a very small time step dt. Then, the method is restricted by stability rather than by accuracy. The presence of this large eigenvalue, together with small eigenvalues, indicates that the problem is
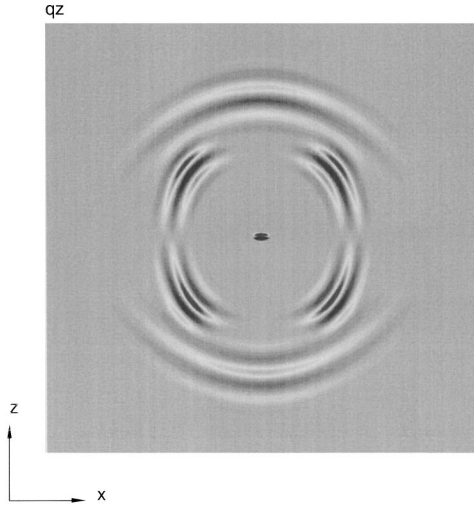
FIG. 6. Snapshot of the q_z particle velocity component for sandstone and $\eta \neq 0$. The static slow wave can be observed at the source location.

stiff.[14] In other words, the eigenvalues have negative real parts and differ greatly in magnitude. In stiff problems, the solution to be computed is slowly varying but perturbations exist that are rapidly damped. In this case, the perturbation is the slow wave, which, in the presence of fluid viscosity, presents a diffusive character.

As mentioned above, the spatial derivatives are calculated with the Fourier method by using the FFT.[23] This approximation is infinitely accurate for bandlimited periodic functions with cutoff spatial wave numbers which are smaller than the cutoff wave numbers of the mesh. The stability problem posed by the eigenvalue $\lambda_s^{(1)}$ can be solved if an A-stable method[14] is used, implying stability in the open left-half-plane. Alternatively, the solution can be obtained with a *partition* method.[22] For instance, consider the low-frequency poroelastic equations. The system can be partitioned into two set of differential equations, one stiff and the other nonstiff, such that they can be treated by two different methods, one implicit and the other explicit, respectively. In the case of Eqs. (38)–(41), the stiff equations

$$\partial_t v_x = -\frac{\eta}{\kappa_1}\beta_{12}^{(1)}q_x, \tag{72}$$

$$\partial_t v_z = -\frac{\eta}{\kappa_3}\beta_{12}^{(3)}q_z, \tag{73}$$

$$\partial_t q_x = -\frac{\eta}{\kappa_1}\beta_{22}^{(1)}q_x, \tag{74}$$

$$\partial_t q_z = -\frac{\eta}{\kappa_3}\beta_{22}^{(3)}q_z, \tag{75}$$

can be solved analytically, giving

$$v_x^* = v_x^n + \frac{\beta_{12}^{(1)}}{\beta_{22}^{(1)}}[\exp(\lambda_s^{(1)}\,dt)-1]q_x^n,$$

$$v_z^* = v_z^n + \frac{\beta_{12}^{(3)}}{\beta_{22}^{(3)}}[\exp(\lambda_s^{(3)}\,dt)-1]q_z^n, \tag{76}$$

$$q_x^* = \exp(\lambda_s^{(1)}\,dt)q_x^n, \quad q_z^* = \exp(\lambda_s^{(3)}\,dt)q_z^n, \tag{77}$$

where $\lambda_s^{(i)} = -(\eta/\kappa_i)\beta_{22}^{(i)}$. Note that, when $\eta = 0$, is $v^* = v^n$ and $q^* = q^n$, giving the purely elastic problem.

The intermediate vector

$$\mathbf{W}^* = [v_x^*, v_z^*, q_x^*, q_z^*, \tau_{xx}^n, \tau_{zz}^n \tau_{xz}^n, p^n]^\mathsf{T} \tag{78}$$

is the input for an explicit high-order scheme that solves Eq. (67) with $\eta = 0$ to give $\mathbf{W}^{n+1}$. The method uses the following 4th-order Runge–Kutta algorithm:[14]

$$\mathbf{W}^{n+1} = \mathbf{W}^* + \frac{dt}{6}(\Delta_1 + 2\Delta_2 + 2\Delta_3 + \Delta_4), \tag{79}$$

where

$$\Delta_1 = \mathbf{M}\mathbf{W}^* + \mathbf{S}^n, \tag{80}$$

$$\Delta_2 = \mathbf{M}\left(\mathbf{W}^* + \frac{dt}{2}\Delta_1\right) + \mathbf{S}^{n+1/2}, \tag{81}$$

$$\Delta_3 = \mathbf{M}\left(\mathbf{W}^* + \frac{dt}{2}\Delta_2\right) + \mathbf{S}^{n+1/2}, \tag{82}$$

$$\Delta_4 = \mathbf{M}(\mathbf{W}^* + dt\Delta_3) + \mathbf{S}^{n+1}. \tag{83}$$

The advantage of the partition method is that the time step is determined by the algorithm that solves the nonstiff equations. The following section considers wave propagation in the sonic band where the low-frequency Biot theory applies. The high-frequency Biot equations will be considered in a future work.

VI. THEORETICAL RESULTS AND SIMULATIONS

Two materials, whose properties are given in Table I, are considered. The values of the first column correspond to a brine saturated sandstone and the values between parentheses refer to a strong anisotropic medium, whose matrix is formed with alternating layers of epoxy and glass.[24] The characteristic frequency ω_c for the x direction is 25 500 Hz.

The theoretical results are obtained from the plane-wave analysis carried out in Sec. IV and the Appendix, in particular from the expressions of the slowness, attenuation and energy velocity curves given by Eqs. (60), (61), and (62), respectively. Figure 1 shows polar representations of (a) the slowness curves and (b) the energy velocity curves for $\eta = 0$, corresponding to the sandstone. Only one quarter of the curves are displayed because of symmetry considerations. The tickmarks indicate the polarization directions, with the points uniformly sampled as a function of phase angle. Since a receiver detects the motion of the bulk material, the plotted polarization is the center of mass particle velocity vector

$$\mathbf{b} = \mathbf{v} + (\rho_f/\rho)\mathbf{q} \tag{84}$$

introduced by Sahay.[25] Referring to Fig. 1(b), the outer curve corresponds to the fast quasicompressional wave, denoted hereafter by qP_1; then follow the quasishear wave qS and the slow quasicompressional wave qP_2 (the opposite order applies to the slowness curves). When $\eta = 0$, there is no dissipation and the curves are frequency independent. As can be seen in Fig. 1(b), qP_1 polarizations are practically normal to the energy velocity curves (or wavefront, if multiplied by 1
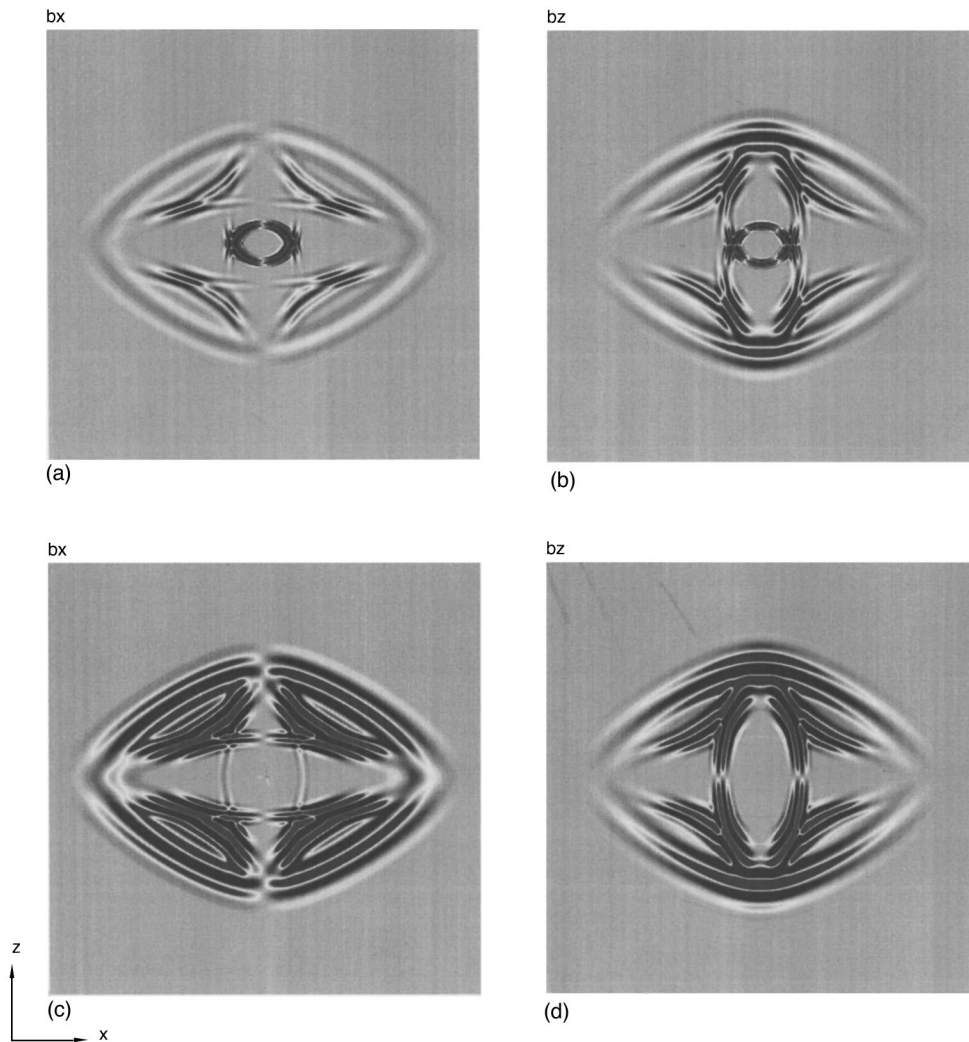
FIG. 7. Snapshots (not scaled) of the center of mass particle velocity components at 1.8-ms propagation time, where (a) and (b) correspond to $\eta=0$, and (c) and (d) to $\eta\neq0$. The medium is epoxy–glass. Three events can be observed, the fast qP_1 wave (outer wavefront), the qS wave and the slow qP_2 wave (inner wavefront).

s), in contrast with qP_2 polarizations, which depart substantially from the normal.

Slowness, attenuation and energy velocity curves for sandstone and $\eta\neq0$ are represented in Fig. 2, where (a) and (b) show the slownesses, (c) and (d) the attenuations, and (e) and (f) the energy velocities. The curves are frequency dependent and correspond to a frequency of 3730 Hz, which is the central frequency of the source used for the numerical simulation. The qP_2 mode presents a diffusive behavior, as can be deduced from the low propagation velocity and very high attenuation, compared to the other waves. The dissipation of the three modes is strongly anisotropic, with the qP_1 and qS modes showing opposite behaviors. Moreover, the qP_2 wavefront is more anisotropic and has a more anomalous polarization behavior compared to the elastic case ($\eta=0$).

Figure 3 shows polar representations of (a) the slowness curves and (b) the energy velocity curves of the three waves, for $\eta=0$, corresponding to the synthetic material. The propagation is very anisotropic, with the qP_2 presenting a quasishear behavior, as can be inferred from the polarizations.

Moreover, this wave shows triplication (cusps) in the horizontal direction. The curves for $\eta\neq0$ and a frequency of 3135 Hz are displayed in Fig. 4, where (a) and (b) show the slownesses, (c) and (d) the attenuations, and (e) and (f) the energy velocities. In particular, note the mixed quasicompressional and quasishear features of the qP_2 cuspidal triangles. Anisotropic tortuosity does not have a major influence on the qP_1 and qS waves, but significantly affects the slow wavefront. This is explained by the fact that the phase velocity of the slow wave is (approximately) inversely proportional to the square root of the tortuosity. The exact inverse proportionality is satisfied for isotropic media and when the fluid bulk modulus is much lower than that of the solid skeleton.[1] In addition, differential permeability enhances the anisotropic behavior of the qP_2 mode, as can be inferred from a comparison of Figs. 3(b) and 4(f).

The numerical mesh for simulating transient propagation has $N_X=N_Z=375$ points, with a grid spacing $D_X=D_Z=5$ cm, and a source central frequency of 3730 Hz for the sandstone and 3135 Hz for the epoxy–glass material. The source is a fluid volume injection (s_f) plus a vertical force (s_{33}),

applied to the drained skeleton, and the wave field is propagated with a time step of 3 μs.

Figure 5 gives snapshots (not scaled) of the center of mass particle velocity components at 1.56-ms propagation time, where (a) and (b) correspond to $\eta=0$, and (c) and (d) to $\eta\neq0$. The medium is sandstone. Three events can be observed, the fast qP_1 wave (outer wavefront), the qS wave and the slow qP_2 wave (inner wavefront). The radiation pattern of this wave differs from that of the fast compressional wave in the horizontal direction, where there is substantial horizontal motion. When the fluid is viscous, the slow wave becomes diffusive and the snapshots resemble those of a single-phase medium. However, a plot of, for instance, the q_z component (Fig. 6), indicates the presence of the static (diffusive) slow mode at the source location. This phenomenon is stronger in the fluid phase.[22]

The snapshots corresponding to the epoxy–glass porous medium are represented in Fig. 7, where (a) and (b) correspond to $\eta=0$, and (c) and (d) to $\eta\neq0$. The propagation time is 1.8 ms. The cuspidal triangles of the qS and qP_2 waves can be clearly appreciated. Moreover, Fig. 7(a) and (b) confirm the results of Fig. 3(b), that, at approximately 45 deg, the polarization of the qP_2 wave is almost horizontal.

ACKNOWLEDGMENT

APPENDIX: ENERGY BALANCE, UMOV–POYNTING VECTOR AND ENERGY DENSITIES

The derivation of the energy balance equation or Umov–Poynting theorem is straightforward when using complex notation. The same procedure given in Carcione and Cavallini[20] for single-phase media is used here. The strain vector corresponding to the plane wave (48) is

$$\mathbf{E}=-\frac{k}{\omega}\mathbf{L}^{\mathsf{T}}\cdot\mathbf{V}. \tag{A1}$$

This vector, with the notation given in Biot,[15] is equal to $\mathbf{E}=[e_x,e_z,\gamma_y,-\zeta]^{\mathsf{T}}$. The dot product of the complex conjugate of Eq. (A1) with $\mathbf{T}^{\mathsf{T}}$ gives

$$-k^*\mathbf{T}^{\mathsf{T}}\cdot\mathbf{L}^{\mathsf{T}}\cdot\mathbf{V}^*=\omega\mathbf{T}^{\mathsf{T}}\cdot\mathbf{E}^*. \tag{A2}$$

On the other hand, the dot product of $-\mathbf{V}^{*\mathsf{T}}$ with Eq. (54) is

$$-k\mathbf{V}^{*\mathsf{T}}\cdot\mathbf{L}\cdot\mathbf{T}=\omega\mathbf{V}^{*\mathsf{T}}\cdot\mathbf{\Gamma}\cdot\mathbf{V}. \tag{A3}$$

The left-hand sides of Eqs. (A2) and (A3) contain the complex Umov–Poynting vector

$$\mathbf{P}=-\frac{1}{2}\begin{bmatrix}\tau_{xx} & \tau_{xz} & -p & 0 \\ \tau_{xz} & \tau_{zz} & 0 & -p\end{bmatrix}\cdot\mathbf{V}^*. \tag{A4}$$

In fact, by virtue of Eq. (49), Eqs. (A2) and (A3) become

$$2\mathbf{k}^{*\mathsf{T}}\cdot\mathbf{P}=\omega\mathbf{T}^{\mathsf{T}}\cdot\mathbf{E}^* \tag{A5}$$

and

$$2\mathbf{k}^{\mathsf{T}}\cdot\mathbf{P}=\omega\mathbf{V}^{*\mathsf{T}}\cdot\mathbf{\Gamma}\cdot\mathbf{V}, \tag{A6}$$

respectively. Adding (A5) and (A6), and using Eq. (49), yields

$$4\boldsymbol{\kappa}^{\mathsf{T}}\cdot\mathbf{P}=\omega(\mathbf{T}^{\mathsf{T}}\cdot\mathbf{E}^*+\mathbf{V}^{*\mathsf{T}}\cdot\mathbf{\Gamma}\cdot\mathbf{V}). \tag{A7}$$

It can be easily shown, from Eqs. (52) and (A1), that the quantity $\mathbf{T}^{\mathsf{T}}\cdot\mathbf{E}^*$ is always real, even when $\eta\neq0$.

The significance of Eq. (A7) becomes clear when one recognizes that each of its terms has a precise physical meaning on a time-average basis. When using complex notation for plane waves, the field variables are obtained as the real part of the corresponding complex field. For two field variables $\mathbf{A}$ and $\mathbf{B}$ of dimension n, the time average of their scalar product over a cycle of period $T=2\pi/\omega$ is given by[26]

$$\langle\mathrm{Re}(\mathbf{A}^{\mathsf{T}})\cdot\mathrm{Re}(\mathbf{B})\rangle=\tfrac{1}{2}\,\mathrm{Re}(\mathbf{A}^{\mathsf{T}}\cdot\mathbf{B}^*). \tag{A8}$$

Then, the time average of the real Umov–Poynting vector

$$-\mathrm{Re}\begin{bmatrix}\tau_{xx} & \tau_{xz} & -p & 0 \\ \tau_{xz} & \tau_{zz} & 0 & -p\end{bmatrix}\cdot\mathrm{Re}(\mathbf{V}) \tag{A9}$$

is

$$\langle\mathbf{P}\rangle=\mathrm{Re}(\mathbf{P}), \tag{A10}$$

which gives the average power flow.

The time average of the strain energy density

$$W=\tfrac{1}{2}\,\mathrm{Re}(\mathbf{T}^{\mathsf{T}})\cdot\mathrm{Re}(\mathbf{E}) \tag{A11}$$

is

$$\langle W\rangle=\tfrac{1}{4}\mathbf{T}^{\mathsf{T}}\cdot\mathbf{E}^*, \tag{A12}$$

since, as stated above, $\mathbf{T}^{\mathsf{T}}\cdot\mathbf{E}^*$ is a real quantity.

Similarly, the average kinetic and dissipated energy densities are given by

$$\langle T\rangle=\tfrac{1}{4}\,\mathrm{Re}(\mathbf{V}^{\mathsf{T}}\cdot\mathbf{\Gamma}\cdot\mathbf{V}^*) \tag{A13}$$

and

$$\langle D\rangle=\tfrac{1}{4}\,\mathrm{Im}(\mathbf{V}^{\mathsf{T}}\cdot\mathbf{\Gamma}\cdot\mathbf{V}^*), \tag{A14}$$

respectively. Equation (A14) represents the energy loss per unit volume of the bulk due to the fluid viscosity.

Substituting Eqs. (A10) and (A12)–(A14) into the real part of Eq. (A7) gives

$$\boldsymbol{\kappa}^{\mathsf{T}}\cdot\langle\mathbf{P}\rangle=\omega(\langle W\rangle+\langle T\rangle)\equiv\omega\langle E\rangle, \tag{A15}$$

where

$$\langle E\rangle=\langle T+W\rangle \tag{A16}$$

is the mean energy density. Defining the energy velocity as in Eq. (62), Eq. (A15) gives

$$\hat{\boldsymbol{\kappa}}^{\mathsf{T}}\cdot\mathbf{V}_e=V_p, \tag{A17}$$

where $V_p=\omega/\kappa$ is the phase velocity. The relation (A17), as in a single-phase medium,[20] means that the phase velocity is simply the projection of the energy velocity onto the propagation direction.

On the other hand, substracting Eq. (A5) from (A6) and using (49) yields the energy balance equation

$$-\boldsymbol{\alpha}^{\mathsf{T}}\cdot\mathbf{P}=\iota\omega[\langle W\rangle-\langle T\rangle]-\omega\langle D\rangle. \tag{A18}$$

Taking the real part of (A18) yields

$$\boldsymbol{\alpha}^{\mathsf{T}}\cdot\langle\mathbf{P}\rangle=\omega\langle D\rangle. \tag{A19}$$

This equation is the generalization of a similar relation for viscoelastic single-phase media,[20] stating that the time-average dissipated energy can be obtained as the projection of the average power flow density onto the attenuation direction.

The Umov–Poynting vector (A10) can be expressed in terms of the eigenvectors $\mathbf{V}$ and complex velocities V obtained from Eqs. (57) and (58), respectively. Defining the matrices

$$\mathbf{U}_1 = \begin{bmatrix} 1 & 0 & 0 & 0 \\ 0 & 0 & 1 & 0 \\ 0 & 0 & 0 & 1 \\ 0 & 0 & 0 & 0 \end{bmatrix} \quad \text{and} \quad \mathbf{U}_3 = \begin{bmatrix} 0 & 0 & 1 & 0 \\ 0 & 1 & 0 & 0 \\ 0 & 0 & 0 & 0 \\ 0 & 0 & 0 & 1 \end{bmatrix},$$
(A20)

the average power flow can be written as

$$\langle \mathbf{P} \rangle = -\tfrac{1}{2} \operatorname{Re}\{[\hat{\mathbf{e}}_x (\mathbf{U}_1 \cdot \mathbf{T})^\mathsf{T} + \hat{\mathbf{e}}_z (\mathbf{U}_3 \cdot \mathbf{T})^\mathsf{T}] \cdot \mathbf{V}^*\}.$$
(A21)

Then, substitution of the constitutive Eq. (52) gives

$$\langle \mathbf{P} \rangle = \tfrac{1}{2} \operatorname{Re}\{V^{-1} \mathbf{V}^\mathsf{T} \cdot \mathbf{C}^\mathsf{T} \cdot [\hat{\mathbf{e}}_x \mathbf{U}_1^\mathsf{T} + \hat{\mathbf{e}}_z \mathbf{U}_3^\mathsf{T}] \cdot \mathbf{V}^*\}.$$
(A22)

The average strain energy density can be further simplified. Substituting Eq. (A1) into Eq. (A12) and using the stress-strain relation (52) yields

$$\langle W \rangle = \tfrac{1}{4} |V|^{-2} \mathbf{V}^\mathsf{T} \cdot \mathbf{C}^\mathsf{T} \cdot \mathbf{L}^\mathsf{T} \cdot \mathbf{V}^*.$$
(A23)

Rewriting Eq. (A23) as

$$\langle W \rangle = \tfrac{1}{4} |V|^{-2} (\mathbf{\Gamma} \cdot \mathbf{\Gamma}^{-1} \cdot \mathbf{L} \cdot \mathbf{C} \cdot \mathbf{V})^\mathsf{T} \cdot \mathbf{V}^*,$$
(A24)

and using (57), yields

$$\langle W \rangle = \tfrac{1}{4} |V|^{-2} V^2 \mathbf{V}^\mathsf{T} \cdot \mathbf{\Gamma} \cdot \mathbf{V}^*,$$
(A25)

where the fact that $\mathbf{\Gamma}$ is a symmetrix matrix has been used. Equation (A25) is formally similar to the strain energy density in single-phase anisotropic-viscoelastic media, where $\langle W \rangle = \tfrac{1}{4} \rho_s |V|^{-2} V^2 |\mathbf{V}|^2$ (see Carcione and Cavallini[27]). In the single-phase medium, every particle velocity component is equally weighted by the density. Note that, when $\eta = 0$, V is real and the average strain energy density equals the average kinetic energy (A13).

From Eqs. (A13) and (A23), the mean energy density (A16) becomes

$$\langle E \rangle = \frac{1}{4} \operatorname{Re}\left[\left(1 + \frac{V^2}{|V|^2}\right) \mathbf{V}^\mathsf{T} \cdot \mathbf{\Gamma} \cdot \mathbf{V}^*\right].$$
(A26)

[1] T. Bourbie, O. Coussy, and B. Zinszner, *Acoustics of Porous Media* (Institut Francais du Petrole, Paris, 1987).

[2] J. F. Allard, *Propagation of Sound in Porous Media: Modelling Sound Absorbing Materials* (Elsevier, London, 1993).

[3] O. Coussy, *Mechanics of Porous Continua* (Wiley, Chichester, 1995).

[4] M. A. Biot, ''Theory of elasticity and consolidation for a porous anisotropic solid,'' J. Appl. Phys. **26**, 182–185 (1955).

[5] M. A. Biot, ''Theory of deformation of a porous viscoelastic anisotropic solid,'' J. Appl. Phys. **27**, 459–467 (1956).

[6] M. A. Biot and D. G. Willis, ''The elastic coefficients of the theory of consolidation,'' J. Appl. Mech. **24**, 594–601 (1957).

[7] M. Thompson and J. R. Willis, ''A reformulation of the equations of anisotropic poroelasticity,'' J. Appl. Mech. ASME **58**, 612–616 (1991).

[8] M. Badiey, I. Jaya, and A. H-D. Cheng, ''Propagator matrix for plane wave reflection from inhomogeneous anisotropic poroelastic seafloor,'' J. Comput. Acoust. **2**, 11–27 (1994).

[9] A. N. Norris, ''Low-frequency dispersion and attenuation in partially saturated rocks,'' J. Acoust. Soc. Am. **94**, 359–370 (1993).

[10] A. Ben Menahem and R. L. Gibson, ''Directional attenuation of SH waves in anisotropic poroelastic media,'' J. Acoust. Soc. Am. **93**, 3057–3065 (1993).

[11] S. Gelinsky and S. A. Shapiro, ''Poroelastic velocity and attenuation in media with anisotropic permeability,'' 64th Ann. Internat. Mtg., Soc. Expl. Geophys., Expanded Abstracts, 818–821 (1994).

[12] S. Gelinsky and S. A. Shapiro, ''Low frequency anisotropy of layered media,'' 57th Ann. Internat. Mtg. Europ. Assoc. Expl. Geophys., Expanded Abstracts, P019 (1995).

[13] M. N. Kazi-Aoual, G. Bonnet, and P. Jouanna, ''Green's functions in an infinite transversely isotropic saturated poroelastic medium,'' J. Acoust. Soc. Am. **84**, 1883–1889 (1988).

[14] M. K. Jain, *Numerical Solutions of Differential Equations* (Wiley Eastern, New Delhi, 1984).

[15] M. A. Biot, ''Mechanics of deformation and acoustic propagation in porous media,'' J. Appl. Phys. **33**, 1482–1498 (1962).

[16] M. A. Biot, ''Theory of propagation of elastic waves in a fluid-saturated porous solid. I. Low-frequency range,'' J. Acoust. Soc. Am. **28**, 168–178 (1956).

[17] A. B. Ben-Menahem and S. J. Singh, *Seismic Waves and Sources* (Springer-Verlag, New York, 1981).

[18] J. L. Auriault, L. Borne, and R. Chambon, ''Dynamics of porous saturated media, checking of the generalized law of Darcy,'' J. Acoust. Soc. Am. **77**, 1641–1650 (1985).

[19] G. Casula and J. M. Carcione, ''Generalized mechanical model analogies of linear viscoelastic behavior,'' Boll. Geofis. Teor. Appl. **34**, 235–256 (1992).

[20] J. M. Carcione and F. Cavallini, ''Energy balance and fundamental relations in anisotropic-viscoelastic media,'' Wave Motion **18**, 11–20 (1993).

[21] J. M. Carcione, ''A 3-D time-domain wave equation for viscoacoustic saturated porous media,'' Eur. J. Mech. A/Solids **12**, 53–71 (1993).

[22] J. M. Carcione and G. Quiroga-Goode, ''Some aspects of the physics and numerical modeling of Biot compressional waves,'' J. Comput. Acoust. **3**, 261–280.

[23] D. Kosloff, M. Reshef, and D. Loewenthal, ''Elastic wave calculations by the Fourier method,'' Bull. Seismol. Soc. Am. **74**, 875–891 (1984).

[24] J. M. Carcione, D. Kosloff, and A. Behle, ''Long-wave anisotropy in stratified media: A numerical test,'' Geophysics **56**, 245–254 (1991).

[25] P. N. Sahay, ''Natural field variables in dynamic poroelasticity,'' 64th Ann. Internat. Mtg., Soc. Expl. Geophys., Expanded Abstracts, 1163–1166 (1994).

[26] H. G. Booker, *Energy in Electromagnetism* (IEE Electromagnetic Waves Series, New York, 1992), Vol. 13.

[27] J. M. Carcione and F. Cavallini, ''Attenuation and quality factor surfaces in anisotropic-viscoelastic media,'' Mech. Mater. **19**, 311–327 (1995).